Optics Letters

All-polarization-maintaining divided pulse fiber oscillator mode-locked with the optical Kerr effect

Marvin Edelmann,[1,2,3,*] Yi Hua,[1,4] Gabor Kulcsar,[5] and Franz X. Kärtner[1,4]

[1]Center for Free-Electron Laser Science CFEL, Deutsches Elektronen-Synchrotron DESY, Notkestr. 85, 22607 Hamburg, Germany
[2]Department of Physics, Universität Oldenburg, Ammerländer Heerstr. 114-118, 26111 Oldenburg, Germany
[3]Cycle GmbH, Notkestr. 85, 22607 Hamburg, Germany
[4]Department of Physics, Universität Hamburg, Jungiusstr. 9, 20355 Hamburg, Germany
[5]Laser Impulse, Wiesenkamp 30, 24226 Heikendorf, Germany
*Corresponding author: marvin.edelmann@desy.de

Received 7 October 2021; revised 8 November 2021; accepted 13 November 2021; posted 15 November 2021; published 14 December 2021

In this Letter, we investigate a Yb-doped mode-locked fiber oscillator that uses coherent pulse division and recombination to avoid excessive nonlinear phase shifts. The mode locking mechanism of the laser is based on the accumulation of a differential nonlinear phase between orthogonal polarization modes in the polarization-maintaining fiber segment. The inserted coherent pulse divider, based on YVO_4 crystals rotated successively by 45°, enables stable and undistorted mode-locked steady states. The output pulse energy is increased from 89 pJ in the nondivided operation by ≈6.5 dB to more than 400 pJ with three divisions. A measurement of amplitude fluctuations reveals a simultaneous broadband noise suppression of up to ≈9 dB in the frequency range from 10 kHz to 2 MHz.

https://doi.org/10.1364/OL.445410

Applications for mode-locked fiber oscillators include many scientific fields and state-of-the-art technologies, such as frequency metrology [1], seeding high-power amplifiers [2], synchronization and timing distribution [3], and optical microwave generation [4]. Rapid progress in these applications necessitates a continuous improvement of fiber oscillators in terms of environmental stability and output characteristics, such as the obtainable pulse energy and noise performance. A key component of an ultrafast fiber oscillator is the saturable absorber (SA), which often determines the cavity structure and the achievable output parameters [5–7]. Among the variety of mode locking mechanisms, *artificial* SAs based on the optical Kerr effect, once environmentally stably implemented, are promising candidates for many applications, based on polarization-maintaining (PM) fibers [8], self-starting operation [9], and superior noise performance [10–12]. A well-established technique utilizes asymmetric fiber loops known as nonlinear amplifying loop mirrors (NALMs) or nonlinear optical loop mirrors (NOLMs), often in combination with a nonreciprocal phase bias that is required for self-starting operation [13]. In these variations of a Sagnac interferometer, the self-amplitude modulation has its origin in the accumulation of a nonlinear phase difference between counterpropagating pulses in the fiber loop [14]. More than 20 years earlier, Fermann *et al.* [15] proposed an alternative linear cavity structure that allows Kerr-type mode locking by using copropagating orthogonal polarization modes in a PM fiber to accumulate the required nonlinear phase difference with a compensation of linear phase shifts. Despite the advantages of the mentioned Kerr-type mode-locked oscillator structures in the all-PM configuration, their performance is still fundamentally limited by the roundtrip nonlinear phase shift and the occurrence of multiple pulse formation owing to soliton splitting or wave breaking if the pulse energy exceeds a certain threshold [16,17]. The achievable intracavity power further restricts the pulse energy and the laser noise performance in terms of phase noise, timing jitter, and amplitude fluctuations at the output [18–20]. Different approaches have been proposed to reduce the roundtrip nonlinear phase shift and scale up the energy. Besides scaling the fiber core size with the implementation of large-mode area (LMA) fibers [21], it is possible to introduce a large breathing ratio of the pulse duration and thus reduce the nonlinear phase shift per roundtrip by accessing the dissipative or dispersion-managed soliton regime through, respectively, an engineered all-normal dispersion or a net dispersion close to zero [22,23]. In 2014, Lamb *et al.* [24] further proposed the application of a coherent divided pulse amplification (DPA) scheme to reduce the pulse peak power in a non-PM, semiconductor saturable absorber mirror (SESAM) mode-locked oscillator, leading to a significant increase in the output pulse energy. While the concept of DPA is routinely used in amplifier systems nowadays [2,25], no information is as yet available on the possibility of a stable implementation within an all-PM oscillator cavity with artificial SA. Consequently, in this Letter we demonstrate and investigate, for the first time to our knowledge, the implementation of a coherent division and recombination scheme in such an all-PM cavity structure to increase the obtainable pulse energy and improve the noise performance. The Kerr-type SA mechanism is based on the accumulation of a differential nonlinear phase shift $\Delta\varphi_{nl}$ between orthogonal polarization modes in the PM fiber segment, as proposed in Ref. [15]. The sinusoidal system transmission function $T(\Delta\varphi_{nl})$, in combination with a nonreciprocal phase bias, allows for stable and undistorted mode locking. The implemented pulse divider scheme consists of a number of

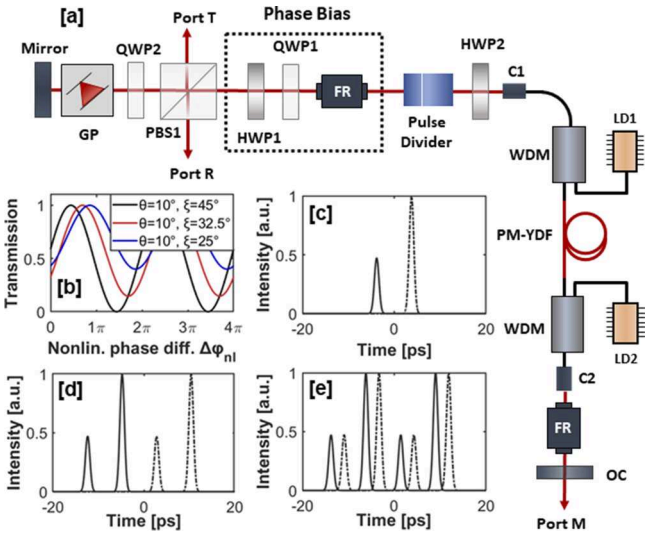

Fig. 1. (a) Experimental setup of the all-PM DPO. GP, grating pair; QWP, quarter-wave plate; PBS, polarizing beamsplitter; HWP, half-wave plate; FR, Faraday rotator; LD, laser diode; WDM, wavelength division multiplexer; YDF, ytterbium-doped fiber; OC, output coupler; C, fiber collimator. (b) Transmission function $T(\Delta\varphi_{nl})$ for different rotation angles of HWP1 (θ) and QWP1 (ξ). (c) Simulated divided pulse train behind the 10 mm YVO_4 crystal (45° rotation to the transmission axis of PBS1) with one pulse parallel to the slow (solid) and fast (dashed) axes for $\theta = 10°$ and $\xi = 25°$. (d) Divided pulses after an additional, 45°-rotated, 20 mm YVO_4 crystal in the divider. (e) Divided pulses at port M with third division from the PM fiber segment.

YVO_4 crystals rotated by 45° in conjunction with a birefringent fiber segment [24]. In the experiment, an increase in output power by up to 6.5 dB is obtained with three pulse divisions, in comparison with the fundamental mode-locked state with no pulse divisions. Measurements of the radio frequency (RF) spectrum and the intensity fluctuations reveal a reduced noise level in the offset frequency range from 10 kHz to ≈2 MHz for an increasing number of divisions.

A schematic of the all-PM divided pulse oscillator (DPO) is shown in Figure 1(a). The 2.2 m fiber segment contains a 0.6 m highly Yb-doped gain fiber (CorActive Yb-401 PM) that is bidirectionally pumped by two 0.9 W laser diodes at 976 nm (Thorlabs BL976-PAG900), coupled into the fiber with wavelength division multiplexers (WDMs). In the free-space arm on the C2 collimator side, the light is transmitted through a 45° Faraday rotator (FR, single pass) and is subsequently partially reflected at the cavity end by an output coupler (OC, 15% transmission) that enables analysis of the divided pulse bursts through the monitor at port M. The fiber output at collimator C1 is followed by the second free-space arm containing a YVO_4 based pulse divider and the nonreciprocal phase bias that consists of a 45° FR, a quarter-wave plate (QWP1) and a half-wave plate (HWP1). A polarization-insensitive transmission grating pair (LightSmyth T-1000-1040 Series) allows tunable dispersion management. The laser is mode-locked in the soliton regime with a fixed net dispersion of $\approx -104 \times 10^{-3}$ ps^2 and a repetition rate of 36.7 MHz. Soliton mode locking is chosen for the experiment to ensure pulse durations of <1 ps in the PM fiber to avoid a timewise overlap of the divided pulses. In the fundamental state of the oscillator without YVO_4 crystals, the orthogonal polarization modes in the PM fiber accumulate a nonlinear phase difference $\Delta\varphi_{nl}$ if there is an asymmetric energy splitting ratio ε [26]. In this case, the value of ε, together with the shape of the sinusoidal SA transmission function $T(\Delta\varphi_{nl})$, is fully determined by the settings of the wave plate angles θ (HWP1) and ξ (QWP1) in the phase bias, as derived, e.g., in Ref. [10]. Besides an accumulation of $\Delta\varphi_{nl}$, the PM fiber's birefringence of $B = 0.381 \times 10^{-3}$ (Coherent PM980-XP) further results in a shift between the polarization modes with ≈1.3 ps/m that is compensated with a Faraday mirror; this ensures an identical optical path for both modes through the 90°-rotated backreflection.

This unique cavity structure enables the application of an YVO_4-based DPA scheme as the intrinsic compensation of linear phase shifts enables the coherent recombination of divided pulses. For the setup in Fig. 1(a), the divider consists of a 10 mm and a 20 mm long YVO_4 crystal in series in combination with the birefringent PM fiber that causes a total delay of ≈2.8 ps. The delay caused by the YVO_4 is ≈0.8 ps/mm at 1030 nm, owing to the large material birefringence of B = 0.208. The fast axis sequential rotation angles in the DPO pulse divider with respect to the transmission axis of the first polarizing beamsplitter (PBS1) for the two YVO_4 crystals and the PM fiber are 45°, 0°, and 45°, respectively. Figure 1(b) shows the resulting shape of $T(\Delta\varphi_{nl})$ for different values of phase bias settings, derived through an implementation of the YVO_4 crystals in the model of Ref. [10] with the corresponding Jones matrices for the birefringent elements. A simulation of the pulse burst after the first 45°-rotated, 10 mm YVO_4 crystal can be seen in Fig. 1(c). The phase bias wave plate angles of $\theta = 10°$ and $\xi = 25°$ ensure an energy splitting ratio of $\varepsilon = 0.8$ with a positive slope of $T(\Delta\varphi_{nl})$ for small signal values of $\Delta\varphi_{nl}$. Figures 1(d) and 1(e) show the simulated divided pulses with two and three divisions after the subsequent, 0°-rotated 20 mm YVO_4 crystals and the PM fiber segment at port M, respectively. The pulse burst in Fig. 1(d) that propagates through the PM fiber segment consists of three identical copies of the fundamental asymmetric pulse pair with identical nonlinear propagation characteristics and accumulated nonlinear phase difference $\Delta\varphi_{nl}$.

In the fundamental mode-locked state, the oscillator generates soliton-like pulses with an output energy of 89 pJ measured at port T with a QWP2 rotation angle that ensures an output coupling ratio of 30%. Figure 2(a) shows the spectrum of the pulse with approximately 8.2 nm FWHM centered at 1038 nm. Figure 2(b) shows the autocorrelation (AC) trace of the pulse burst measured at port M with approximately 2.8 ps delay for the orthogonal polarization modes after a single pass through the PM fiber. Simultaneously, the AC trace of a single recombined pulse can be measured at port T with a FWHM of 0.8 ps. The deviation from the transform limit is due to the required external amplification of the port T and port M pulse trains with an auxiliary fiber amplifier to ensure sufficient peak power for the AC measurement.

In this fundamental state, the laser is self-starting at a pump power of approximately 300 mW. Single-pulse operation can be achieved by reducing the pump power to approximately 75 mW. The verification of stable single-pulse operation is based on a number of separate measurements. As a first step, the 150 ps wide-range AC, together with a 0.02 nm high-resolution spectral measurement, is used to ensure the absence of periodic modulations in the spectrum. Further, the pulse train at port T is detected with a fast InGaAs p-i-n photodetector (EOT-3000)

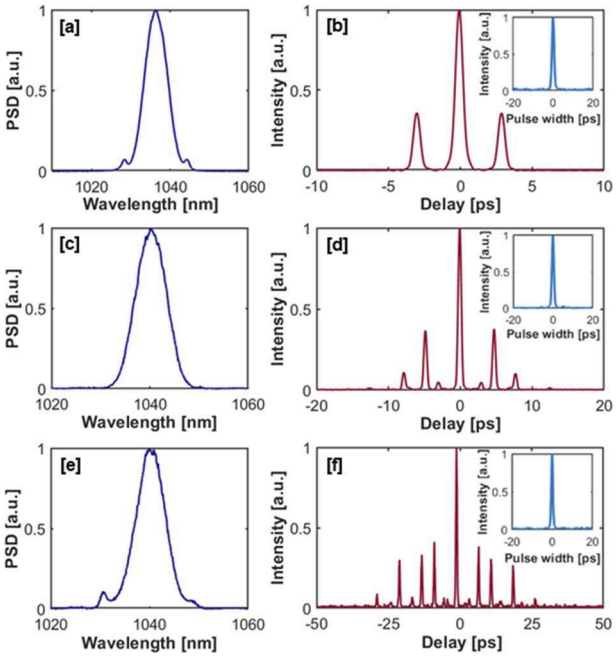

Fig. 2. (a) Spectral bandwidth at port T with FWHM of approximately 8.2 nm for one division in PM fiber. (b) Corresponding pulse burst at port M; the inset shows the autocorrelation of the externally amplified recombined pulse at port T with 0.8 ps duration. (c), (d) Port T spectral bandwidth (8.3 nm FWHM) and pulse burst at port M for two pulse divisions with additional 10 mm YVO_4 crystal, respectively. The recombined pulse at port T [inset to (d)] has a FWHM of 0.83 ps. (e), (f) Port T spectral bandwidth (8.2 nm FWHM) and port M pulse burst autocorrelation for a third division with an additional 20 mm YVO_4 crystal. Inset to (f): recombined and amplified pulse at port T with 0.8 ps FWHM. PSD, power spectral density.

and the RF spectrum is measured with a spectrum analyzer (Keysight N9000A) over the full photodetector bandwidth of 2 GHz (100 kHz resolution) to verify the absence of amplitude modulations of the higher harmonics. Figure 2(c) shows the optical spectrum at port T with a second pulse divider in the cavity. Here, the polarization modes are first separated in the 45°-rotated, 10 mm YVO_4 crystal with a delay of approximately 8 ps and then further divided in the 0°-rotated PM fiber segment. The corresponding autocorrelation of the pulse burst measured at port M is shown in Fig. 2(d), together with the autocorrelation trace of the recombined pulse at port T with a FWHM of 0.83 ps and a pulse energy of approximately 190 pJ. Subtle spectral modulations in conjunction with small perturbations in the AC trace indicate a distorted recombination of the pulse burst, e.g., owing to deviations from ideal divider rotation angles and tolerances of the Faraday mirror. The observed changes of the Kelly sidebands can be explained with a shifting cavity dispersion owing to the additionally implemented YVO_4 crystals, a shifting working point on $T(\Delta\varphi_{nl})$ in the steady state and slightly different gain dynamics owing to the higher intracavity power. Self-starting operation requires an approximately 700 mW pump power, while the single-pulse threshold is at approximately 160 mW. The higher pump power for self-starting operation is required for an accumulation of sufficient small signal $\Delta\varphi_{nl}$ despite the reduction in peak power owing to the pulse division. For the third division, the 20 mm YVO_4 crystal is implemented in the cavity with a 0° rotation angle

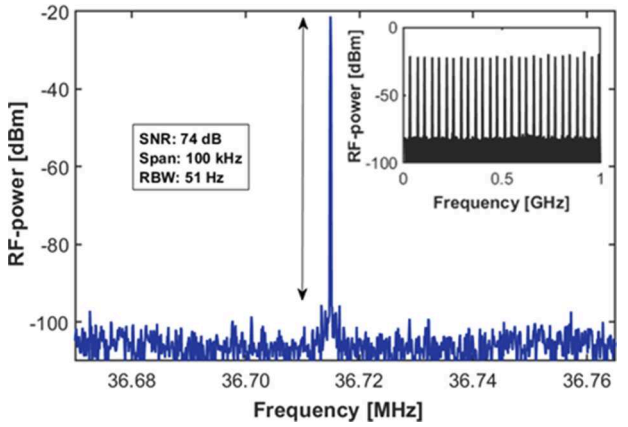

Fig. 3. RF spectrum of the DPO fundamental repetition rate with three divisions at 36.7 MHz measured over a span of 100 kHz with 51 Hz RBW. The SNR is approximately 74 dBm. The inset shows higher harmonics over a 1 GHz span (RBW: 100 kHz).

between the 45°-rotated 10 mm crystal and the 45°-rotated fiber.

The resulting spectral bandwidth (8.2 nm FWHM), together with the corresponding ACs of the pulse burst at port M and that of the recombined pulse at port T (0.8 ps FWHM) can be seen in Figs. 2(e) and 2(f), respectively. For this state, the output pulse energy is increased by 6.5 dB to 400 pJ, compared with the fundamental operation. Starting the laser in this state requires a pump power of up to 1.5 W with the single-pulse threshold at 400 mW. Further divisions were not possible in the experiment, owing to the lack of available pump power for initiation of mode locking.

A significant aspect for the analysis of the DPO characteristics is the influence of each consecutive pulse division on the overall cavity stability and noise performance. Figure 3 shows the RF spectrum of the fundamental frequency of 36.7 MHz measured at port T with three pulse divisions corresponding to the working point shown in Figs. 2(e) and 2(f). The signal-to-noise ratio (SNR) is approximately 74 dBm with a span of 100 kHz and a resolution bandwidth (RBW) of 51 Hz. The inset of Fig. 3 shows the broadband RF spectrum with a span of 1 GHz measured with a RBW of 100 kHz. Furthermore, the amplitude noise (AM noise) of the recombined pulse train emitted at port T for different division states of the oscillator is measured using the method described in Ref. [26]. Once the optical pulse train has been converted to the electrical RF domain with a fast photodetector (EOT-3000), the 5th harmonic at 183.5 MHz of the received RF signal is filtered with a tunable bandpass filter and amplified with a 10 dB transimpedance amplifier to an RF power of −1 dBm, which is kept consistent for all measurements. The AM noise function of the signal source analyzer (SSA, Keysight E5052B) is used to measure the single-sideband noise spectral density. Experimental results of the AM noise measurements at port T in the range from 100 Hz to 20 MHz are shown in Fig. 4(a) for different numbers of pulse divisions. In the high-frequency range from 100 kHz to approximately 3 MHz the AM noise is significantly reduced (by up to 3 dB) with two pulse divisions in the cavity and by up to 6 dB with three divisions, most probably because of the increased intracavity power, as proposed in Ref. [18]. The AM noise reduction is also present in the mid-frequency range from 10 kHz to 100 kHz by up to 9 dB with the

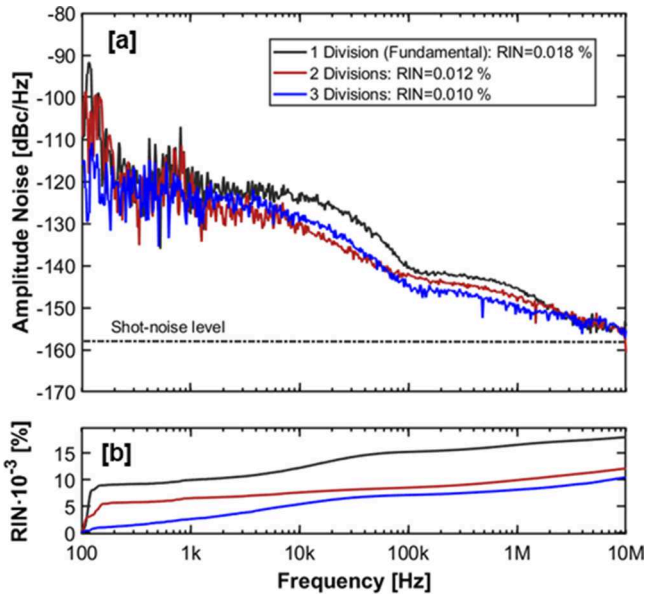

Fig. 4. (a) Frequency-resolved AM noise spectra measured at port T with different pulse divisions in the cavity. (b) Corresponding RIN integrated from 100 Hz to 10 MHz for the fundamental state, two divisions, and three divisions with RIN values of 0.018%, 0.012%, and 0.010%, respectively.

10 mm crystal in the YVO_4 divider and up to 7 dB for the third division with the additional 20 mm crystal. Figure 4(b) shows the corresponding relative intensity noise (RIN) integrated from 100 Hz to 20 MHz, excluding the influence of technical noise sources <100 Hz. For the fundamental mode-locked state, the RIN has a value of 0.018% that is consecutively reduced to 0.012% and 0.010% for the second and third divisions, respectively. The observable AM noise variation for higher divisions can be explained through the averaging character of the coherent recombination. It is further influenced by the interplay between a shifting operation point away from the lasing threshold for more divisions, resulting in an increased stability, as shown in Ref. [27], and occurring changes of the port T noise transfer owing to a shifting working point on $T(\Delta\varphi_{nl})$ [12].

In conclusion, an all-PM Kerr-type fiber oscillator is investigated that uses periodic pulse division and recombination to reduce excessive roundtrip nonlinear phase shifts. The implementation of birefringent pulse division is enabled, owing to the linear cavity structure with intrinsic compensation of linear phase shifts based on a Faraday mirror. In the experiment, the output pulse energy is increased by 6.5 dB from 89 pJ in the fundamental state to more than 400 pJ with three divisions. The stability of the mode-locked DPO for different divisions is investigated based on RF characteristics and the AM noise of the output pulse train. The measured AM noise is found to be reduced by up to 6 dB in the high offset frequency range from 100 kHz to 3 MHz. The increased pulse energy, in conjunction with significantly improved noise performance of the DPO, is another step toward ultralow noise fiber laser systems.

Funding. Deutsche Forschungsgemeinschaft (KA 908/9-1 MUJHO); European Research Council (609920).

Disclosures. The authors declare no conflicts of interest.

Data availability. Data underlying the results presented in this paper are not publicly available at this time but may be obtained from the authors on reasonable request.

REFERENCES

1. B. R. Washburn, S. A. Diddams, N. R. Newbury, J. W. Nicholson, M. F. Yan, and C. G. Jørgensen, Opt. Lett. **29**, 250 (2004).
2. M. Müller, C. Aleshire, A. Klenke, E. Haddad, F. Légaré, A. Tünnermann, and J. Limpert, Opt. Lett. **45**, 3083 (2020).
3. M. Xin, K. Şafak, M. Peng, A. Kalaydzhyan, W. Wang, O.D. Mücke, and F. X. Kärtner, Light: Sci. Appl. **6**, e16187 (2017).
4. R. Bouchand, X. Xie, M. Giunta, W. Hänsel, M. Lezius, R. Holzwarth, C. Alexandre, P. Tremblin, G. Santarelli, and Y. Le Coq, IEEE Photonics Technol. Lett. **29**, 1403 (2017).
5. C.-J. Chen, P. K. A. Wai, and C. R. Menyuk, Opt. Lett. **20**, 350 (1995).
6. V. J. Matsas, D. J. Richardson, T. P. Newson, and D. N. Payne, Opt. Lett. **18**, 358 (1993).
7. L. A. Gomes, L. Orsila, T. Jouhti, and O. G. Okhotnikov, IEEE J. Sel. Top. Quantum Electron. **10**, 129 (2004).
8. J. Szczepanek, T. M. Kardaś, M. Michalska, C. Radzewicz, and Y. Stepanenko, Opt. Lett. **40**, 3500 (2015).
9. D. Kim, D. Kwon, B. Lee, and J. Kim, Opt. Lett. **44**, 1068 (2019).
10. A. S. Mayer, W. Grosinger, J. Fellinger, G. Winkler, L. W. Perner, S. Droste, S. H. Salman, C. Li, C. M. Heyl, I. Hartl, and O. H. Heckl, Opt. Express **28**, 18946 (2020).
11. Y. Ma, S. H. Salman, C. Mahnke, Y. Hua, S. Droste, J. Fellinger, A. S. Mayer, O. H. Heckl, C. M. Heyl, and I. Hartl, J. Lightwave Technol. **39**, 4431 (2021).
12. M. Edelmann, Y. Hua, K. Şafak, and F. X. Kärtner, Opt. Lett. **46**, 1752 (2021).
13. W. Hänsel, H. Hoogland, M. Giunta, S. Schmid, T. Steinmetz, R. Doubek, P. Mayer, S. Dobner, C. Cleff, M. Fischer, and R. Holzwarth, Appl. Phys. B: Lasers Opt. **123**, 41 (2017).
14. N. Nishizawa, H. Suga, and M. Yamanaka, Opt. Express **27**, 19218 (2019).
15. M. E. Fermann, L.-M. Yang, M. L. Stock, and M. J. Andrejco, Opt. Lett. **19**, 43 (1994).
16. R. S. Fodil, F. Amrani, C. Yang, A. Kellou, and P. Grelu, Phys. Rev. A **94**, 013813 (2016).
17. J. Peng, L. Zhan, S. Luo, and Q. Shen, J. Lightwave Technol. **31**, 2709 (2013).
18. R. Paschotta, Opt. Express **18**, 5041 (2010).
19. R. Paschotta, Appl. Phys. B: Lasers Opt. **79**, 163 (2004).
20. H. A. Haus and A. Mecozzi, IEEE J. Quantum Electron. **29**, 983 (1993).
21. W. Liu, H. Shi, J. Cui, C. Xie, Y. Song, C. Wang, and M. Hu, Opt. Lett. **43**, 2848 (2018).
22. J. W. Nicholson and M. Andrejco, Opt. Express **14**, 8160 (2006).
23. A. Chong, J. Buckley, W. Renninger, and F. Wise, Opt. Express **14**, 10095 (2006).
24. E. S. Lamb, L. G. Wright, and F. W. Wise, Opt. Lett. **39**, 2775 (2014).
25. S. Zhou, F. W. Wise, and D. G. Ouzounov, Opt. Lett. **32**, 871 (2007).
26. M. Edelmann, Y. Hua, K. Şafak, and F. X. Kärtner, Opt. Lett. **46**, 3344 (2021).
27. L. Matos, O. D. Mücke, J. Chen, and F. X. Kärtner, Opt. Express **14**, 2497 (2006).